Plasmonics (2021) 16:1633–1644
https://doi.org/10.1007/s11468-021-01431-8

Multiple-Mode Bowtie Cavities for Refractive Index and Glucose Sensors Working in Visible and Near-infrared Wavelength Ranges

Yuan-Fong Chou Chau[1]

Received: 9 February 2021 / Accepted: 15 March 2021 / Published online: 21 March 2021

Abstract
A multiple-mode metal-insulator-metal plasmonic sensor with four coupled bowtie resonators containing two pairs of silver baffles is numerically investigated using the finite element method and verified by the temporal coupled mode theory. The proposed structure can function as a plasmonic refractive index and glucose sensors working in visible and near-infrared wavelength ranges. Simulation results show that introducing the silver baffles in bowtie cavities can modify the plasmon resonance modes and give a tunable way to enhance the sensitivity and figure of merit. The highest sensitivity (S) can reach $S = 1500.00$, 1400.00, and 1100.00 nm/RIU and the high figure of merit (FOM) of 50.00, 46.67, and 36.67 RIU^{-1} from mode 1 to mode 3. The sensitivity obtained from three modes with operating wavelengths in visible and near-infrared simultaneously exceeds 1100.00 nm/RIU along with remarkably high FOM, which are not attainable from other reported literature. The proposed structure can realize multi-mode and shows impressive practical prospects that can be applied for integrated optics circuits (IOCs) and other nanophotonics devices.

Keywords Metal-insulator-metal · Plasmonic sensor · Bowtie resonator · Silver baffle · Finite element method

Introduction

Surface plasmon polaritons (SPPs) are electromagnetic (EM) wave coupled to the collective oscillations of free electrons on the metal surface and propagate between the metal-dielectric interface [1–8]. Plasmonic metal-insulator-metal (MIM) waveguide, one of the SPP waveguide schemes, has received fascinated attentions because of its attractive features, such as bonding strongly localized surface plasmon resonance (SPR), overcoming diffraction limit in conventional optics, low propagation loss, simple manufacturing steps, and compatible integration optics circuits (IOCs) [5, 9–15]. Therefore, a variety of functional plasmonic components utilizing MIM waveguides have been designed experimentally and demonstrated theoretically, such as sensors [16], all-optical switches [17], splitters [18], modulators [19], demultiplexers [20], filters [21], interferometers [22], etc. A plasmonic MIM waveguide consists of the cavities (i.e., resonators) and the bus waveguides [7, 11, 17, 20, 23–31]. The MIM waveguides' cavities greatly impact the SPP modes and resonance conditions because they can support an excellent mechanism for achieving wavelength and sensing selective. In other words, the SPR, cavity plasmon resonance (CPR), and gap surface plasmon resonance (GPR) properties of the plasmonic cavity-waveguide system pick out the specific operating wavelength which required exactly [1, 9, 32–37].

In SPP sensors, the resonance modes generate in the bus waveguide coupled with the cavity under satisfying the Fabry–Pérot resonance condition. The SPP wave can be reflected back and forth in the cavity, which is highly sensitive to the refractive index's change in the bus waveguide and the cavity's geometrical shape. Resonators (or cavities) with different structural configurations undergo a potential role in generating a better light-matter interaction in the MIM-cavity waveguide system [38–40]. Recently, several MIM waveguides with different shape of cavities have been proposed and investigated for the plasmonic sensor, such as rectangular/circular ring cavity [41], tooth-shaped cavity [42], trapezoid cavity [43], ring cavity with metal baffles [44], asymmetric double elliptic cylinders [45], Bragg grating cavity [46], fillet cavity [47], metallic nanorods in

✉ Yuan-Fong Chou Chau
a0920146302@gmail.com

[1] Centre for Advanced Material and Energy Sciences, Universiti Brunei Darussalam, Tungku Link, Gadong BE1410, Negara Brunei Darussalam

hexagonal configuration [48], stub coupled with a square cavity [49], and so forth.

One of the cavity schemes is the bowtie (BT)-shaped resonator, which has an excellent light-matter coupling between the incident EM wave and nanostructures. For example, BT nanoantennas [50–53] possess the advantage of hybrid SPR, CPR, and GPR modes in a plasmonic nanostructure system and are less discussed in the plasmonic MIM-cavity system. This paper numerically investigated the optical properties of a multi-mode waveguide configuration consisting of two MIM bus waveguides connected with the centrally coupled BT cavities containing the silver (Ag) baffles. The finite element method (FEM) systematically simulates BT cavities' resonance modes in the proposed structure. We focus on the flexible optical characteristics of this plasmonic sensor structure for sensing applications (e.g., a glucose sensor). The resonance wavelength-shift features of resonant modes in the BT-shaped cavity inspected by the temporal coupled-mode theory are verified [54]. The calculated transmittance spectra have also been investigated by analyzing the magnetic and electric field's spatial distributions at the resonant wavelengths. The sensitivity analysis of the SPP modes is calculated for two cavity schemes, i.e., the BT cavities excluding and including the Ag baffles. The influence of the geometrical dimension and coupling distance corresponding to the transmittance features was also calculated. The effects of the structural parameters' variation on its sensing characteristics, refractive index sensitivity, figure of merit, and quality factor are calculated. The proposed device sensor can achieve multiple modes working in visible and infrared and could be used as practical nanophotonic devices that functionally perform as chemical sensors and biosensors. This study suggests a promising design strategy and improves the plasmonic sensors on the nanoscale and examines their performance before realizing to time-consuming and expensive IOC construction.

Structure and Basics

Figure 1 shows the schematic two-dimensional (2D) plot of the proposed plasmonic refractive index sensor that consists of two bus waveguides (width w) and four coupled BT cavities (bottom length $L=6w$ and height $H=5w$) containing two pairs of silver baffles in the BT cavities. We termed the Ag baffles as pair 1 in x-direction and pair 2 in the y-direction. The length and width of the bigger Ag baffles in pair 1 and pair 2 are $3w$ and $2w$, while the length and width of the smaller Ag baffles in pair 1 and pair 2 are set the same value of w. The center to center distance of bigger and smaller Ag baffles is fixed as $2w$. The gap distance between the coupled cavities and the bus waveguides is set as g, while the gap distance among four BT cavities is d. Simulations were performed by a 2D FEM using COMSOL Multiphysics [34, 55] with perfectly matched layer absorbing boundary conditions for absorbing outgoing EM waves surrounding the input and output ends. Besides, scattering boundary conditions (SBC) are used at the FEM simulation window's outer edges. It should be noted that a 3D simulation model is simplified to a 2D one because the similar results will be obtained from both models in simulations [40, 56] and experiments [37, 57]. Besides, the 2D simulation can shorten the working time and reduce the required computer resources, without losing the precision [58, 59]. In COMSOL simulations, the proposed structure's subdomains are divided into triangular mesh elements with a fine mesh grid size for the MIM-cavity waveguide geometries. This setting permits us to achieve accurate calculation results within the available computer resources.

A TM-polarized incident EM wave is coupled with the fundamental SPP mode [60] into the bus waveguide's input end. The transmittance (T) can be described as $T=(S_{21})^2$, where S_{21} is the transmittance. In a real situation, the incident EM wave can be coupled into the bus waveguide by photonic crystal fiber (PCF) [61, 62]. Confocal Raman microscopy can measure the output EM wave. The frequency-dependent

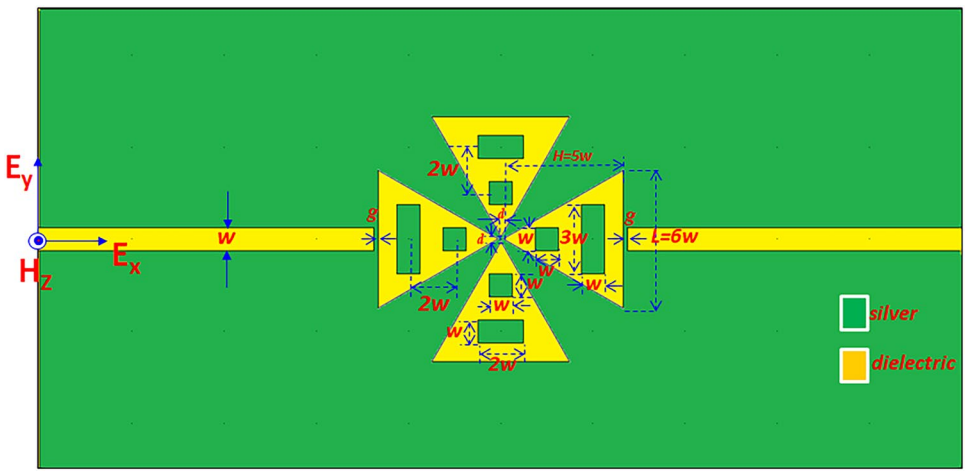

Fig. 1 Schematic 2D diagram of the proposed plasmonic refractive index sensor consisting of two bus waveguides (width w), four coupled BT cavities, including two pairs of Ag baffles in the BT cavities

complex relative permittivity ε_m of silver can calculate using the Drude model as [63]

$$\varepsilon_m(\omega) = \varepsilon_\infty - \frac{\omega_p^2}{\omega^2 + i\omega\gamma} \quad (1)$$

where ε_∞ (the dielectric constant at the infinite angular frequency) = 3.7, ω is the angular frequency of incident light, ω_p (bulk plasma frequency) = 9.10 eV = 1.38×10^{16} rad/s, and γ (the electron collision frequency concerning loss) = 18 meV = 2.7×10^{13} rad/s. The resonance wavelength (λ_{res}) can be obtained from the temporal coupled mode theory [64]. When the SPPs propagate through the proposed structure, they will be confined in the cavity to produce an oscillation. The cavity including Ag baffles can play as a Fabry-Pérot cavities. The gathered phase change per cycle in the cavities can be expressed as $\Delta\varphi = 4\pi n_{eff}\ell_{eff}/\lambda + \varphi$, where n_{eff} is the effective refractive index of the SPPs, ℓ_{eff} is the effective lengths of cavity, φ is the phase shift generated from the reflection at the metal-dielectric interface in the cavity, respectively. If $\Delta\varphi = 2\pi j$ (j is an integer), the resonance wavelength λ_{res} of the cavity can be described by temporal coupled mode theory.

$$\lambda_{res} = \frac{2\ell_{eff} Re(n_{eff})}{j - \frac{\varphi}{2\pi}} (j = 1,2,3\ldots) \quad (2)$$

$Re(n_{eff})$ represents the real part of the effective refractive index obtained from the dispersion equation [65].

Furthermore, sensitivity (S) and figure of merit (FOM) are potential characteristics extensively used to evaluate the sensor performance. The definition of sensitivity is $S = \Delta\lambda/\Delta n$ nanometer per refractive index (nm/RIU), where $\Delta\lambda$ is the shift of the resonant wavelength of transmittance, λ_{res} is the resonant wavelength at transmittance peak, and Δn is the change in the refractive index of the medium in the space of bus waveguides and BT cavities. The figure of merit (FOM) and quality factor (Q factor) can be defined as S/FWHM and λ_{res}/FWHM, respectively, where FWHM is the full width at half-maximum of the transmittance peak.

The fabrication of the proposed plasmonic structure is attainable with prevalent nanotechnologies, such as e-beam lithography, electron-beam deposition, thermal evaporation, and chemical etching. It is well known that the e-beam lithography will enable to create the BT and the baffles and then deposit the silver. The other feasible method can deposit Ag's thin layer on a silica substrate utilizing E-beam deposition or thermal evaporation, which can inscribe desired patterns [66, 67]. To fabricate MIM bus waveguides, we can remove Ag metal's unwanted parts using chemical etching [27, 68-70].

Simulation Results and Discussions

First, we compare the transmittance spectrum of the SPP mode for two cavity configurations, i.e., the BT cavities excluding and including the Ag baffles as shown in Fig. 2. The structural parameters and the related sizes are denoted

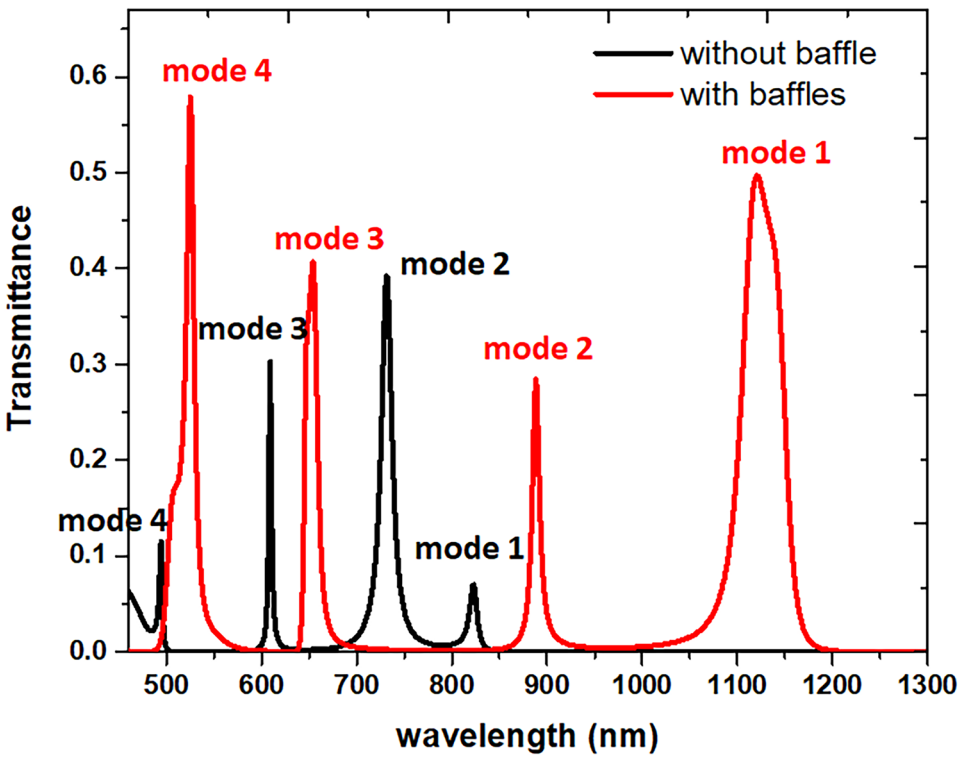

Fig. 2 Transmittance spectra of the proposed plasmonic sensor excluding (black color) and including (red color) Ag baffles in the BT cavities

in Fig. 1. The initial values w, g, and d are 50 nm, 10 nm, and 10 nm, and air ($n = 1$) is used as a medium in the bus waveguides and BT cavities. Note that the bus waveguide width (w) is set as 50 nm to ensure that the fundamental mode can be excited in the bus waveguide. The proposed plasmonic sensor can function as band-pass and band-stop filters, limiting and prohibiting propagating specific incident EM wave wavelengths. An apparent discrepancy after the Ag baffles is included in the plasmonic BT-cavity waveguide system, and the different resonance modes formed in the BT cavities can explain this difference. In Fig. 2, the two cases' transmittance spectrum shows discrete peaks and behaves as a multiple-mode plasmonic filter, leading to the EM wave that can be transmitted at the resonance wavelength (λ_{res}). The transmittance reached a peak value when the SPP modes satisfied the resonance condition in the BT cavities. There are four transmittance peaks found at $\lambda_{res} = 823$ nm, 731 nm, 609 nm, and 494 nm (denoted by mode 1 to mode 4, hereafter) for the case excluding Ag baffles and four modes at $\lambda_{res} = 1121$ nm, 888 nm, 654 nm, and 525 nm for the case including Ag baffles, respectively. It is evident that the transmittance peaks of the case excluding Ag baffle are weaker than the case including Ag baffles, i.e., the case including Ag baffles reveals better light-matter interaction than the case excluding Ag baffle. Besides, the working wavelengths of the case excluding Ag baffle exist in the visible wavelength range.

In contrast, the Ag baffle case's working wavelengths can be reshifted to visible and infrared. These results can be ascribed to the different degree of resonant modes that occurred in the BT cavities. It can be interpreted from Eq. (2) that λ_{res} is closely related to n_{eff} and ℓ_{eff} of the BT cavities. Ag baffles in the BT cavities can generate a larger n_{eff} and increase λ_{res} (i.e., redshift).

To explain the physical mechanism, Figs. 3 and 4 show the steady state of the magnetic field ($|H|$) and electric field ($|E|$) distributions of the case excluding Ag baffles (Figs. 3a–d and 4a–d) and including Ag baffles (Fig. 3e–h and 4e–h) in the BT cavities at corresponding λ_{res} from mode 1 to mode 4, respectively. The BT cavities can regard as the Fabry-Pérot cavities, i.e., optical waves can pass through the optical cavities only when resonating with it. The inclusion of Ag baffles in BT cavities allows the strong confinement of SPPs formed among the gaps of Ag baffles and BT's sharp tips, as shown in Figs. 3 and 4. In Fig. 3, the $|\boldsymbol{H}|$ field intensities show strong field confinement inside the BT cavities, a magnetic dipole resonance feature. In

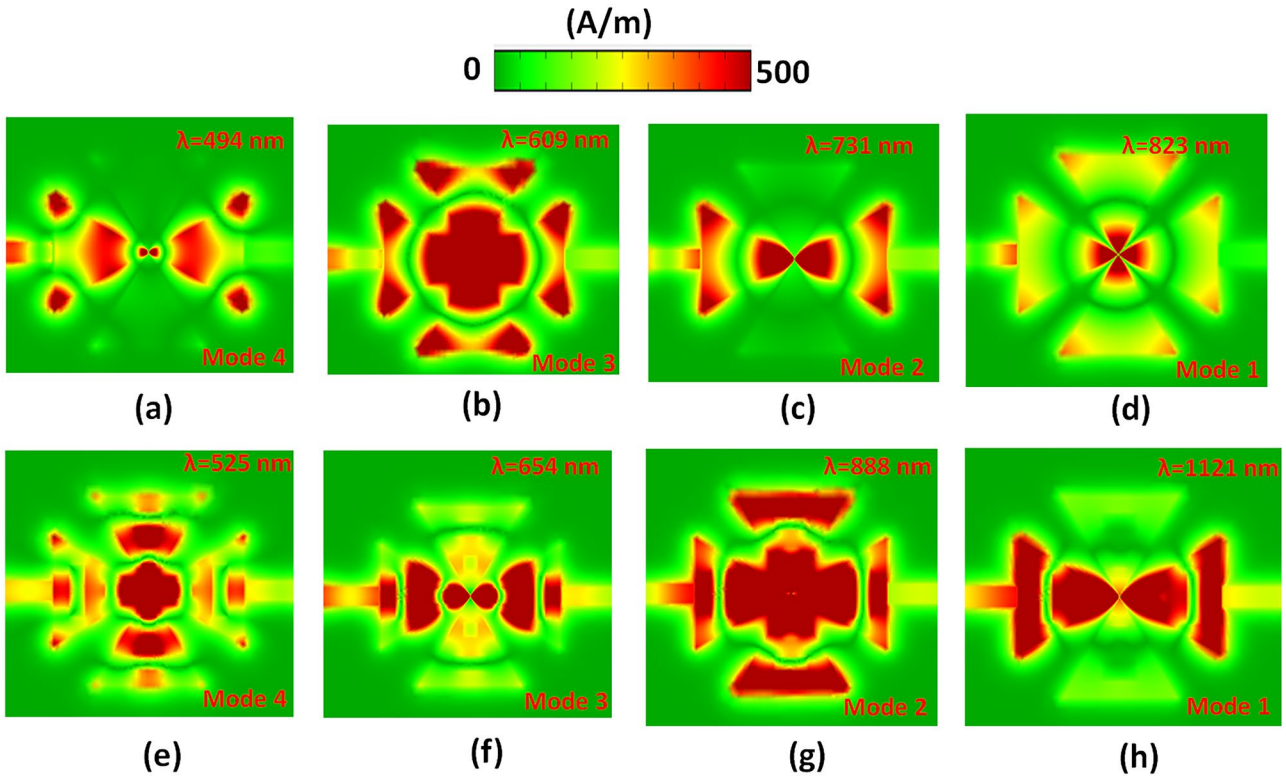

Fig. 3 Truncate views of magnetic field intensity ($|H|$) of (**a**–**d**) the case excluding Ag baffles and (**e**–**h**) including Ag baffles in the BT cavities at corresponding resonance wavelengths from mode 1 to mode 4, respectively

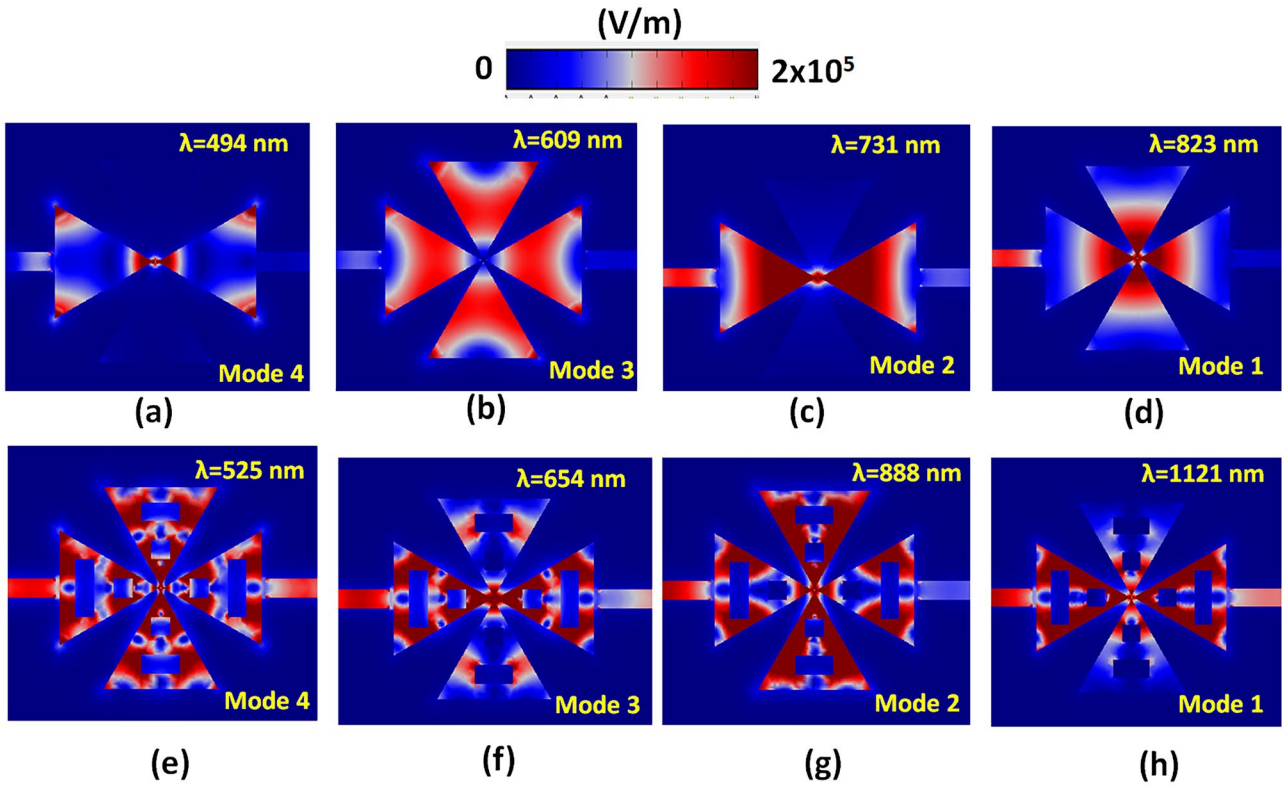

Fig. 4 Truncate views of electric field intensity (|*E*|) of (**a**–**d**) the case excluding Ag baffles and (**e**–**h**) including Ag baffles in the BT cavities at corresponding resonance wavelengths from mode 1 to mode 4, respectively

contrast, the |***E***| field intensities can enhance at the edge and sharp surface of the Ag nanometals, showing a signature of electric field dipole resonance (see Fig. 4). It is worth noting that the |***H***| and |***E***| field profiles offer different distribution patterns in the BT cavities depending on the different incident wavelengths at λ_{res}. It is evident from Figs. 3 and 4 that the SPP wave is coupled to the BT cavities well at λ_{res}, which can form the standing-wave patterns between the bus waveguide and the BT cavities. The |***E***| profiles as shown in Fig. 4a–h exhibit standing wave-like EM wave patterns on the surface of Ag baffles and Ag wall of BT cavities with a remarkable field enhancement since the hybridization of SPR, GPR, and CPR [71, 72]. Ag baffles' case facilitates the stronger SPP mode confinement on the metal surface than the case excluding Ag baffles due to the GPR. The gap regions formed in BT cavities are among the Ag baffles and the wall of BT cavities. High sensitive SPP modes can confine among the gap. As shown in Fig. 4a–h, the electric field intensity can reach its maximum value at the gap regions and sharp edges. SPPs modes in the BT cavities have substantial field enhancements and can constrain the EM waves to the nanometer scale. This critical observation implies that the gap and cavity plasmon resonances can significantly contribute to the field enhancement in the proposed plasmonic BT cavity system including the Ag baffles.

Figures 3 and 4 provide high confinement of |*H*| and |*E*| field distributions of SPP mode in the narrow region between BT cavities and Ag baffles. Consequently, the n_{eff} of the mode increases and is highly responsive to the surrounding medium. When the proposal plasmonic sensor system includes the testing medium, the n_{eff} of the bus waveguide and BT cavities is changed. Therefore, λ_{res} experiences a redshift. SPP modes are highly sensitive to the variation of the surrounding refractive index, which will change λ_{res}, intensity, or phase. Based on Fig. 2, we can use the proposed structure as a refractive index sensor. We can fill the testing medium in the bus waveguides and BT cavities with the different refractive index. Figures 5a, b compare the proposed plasmonic sensors' transmittance spectra excluding and including Ag baffles in the BT cavities. The refractive index of the test medium, n, is set to be 1.01, 1.03, 1.13, and 1.15, respectively, and other ranges of refractive index values have the same trend of transmittance spectrum. The other structural parameters, w, and g are 50 nm and 10 nm, respectively. As seen in Fig. 5, both cases' transmission peaks redshift with the increasing refractive index due to the rising n_{eff} in the BT cavities, giving a linear relationship between wavelength shift with n of the medium being tested. This result is in good agreement

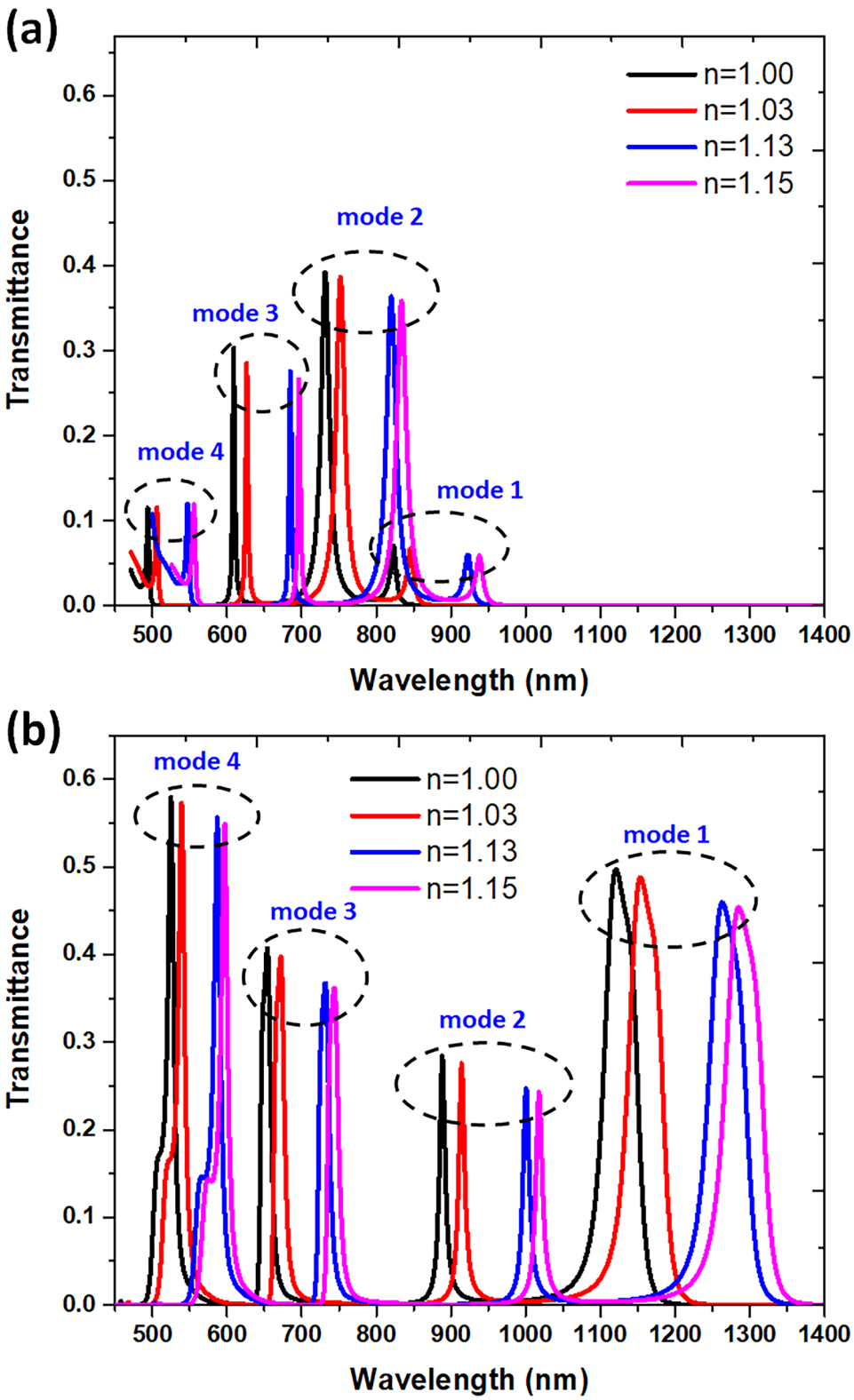

Fig. 5 Transmittance spectra of the proposed plasmonic sensors (**a**) excluding and (**b**) including Ag baffles in the BT cavities. The test medium's refractive index, n, is set as 1.01, 1.03, 1.13, and 1.15, respectively. The other structural parameters, w and g, are 50 nm and 10 nm, respectively

with Eq. (2). The increasing redshift is because of the enhancing EM wave in a BT cavity, mostly interacting with the refractive index change. Since there is a hybridization of the SPR, GPR, and CPR modes in the BT-cavity waveguide system, a little refractive index change (Δn) leads to a remarkable λ_{res} shift.

Figure 6 shows the calculated resonance wavelength (λ_{res}) versus the refractive index (n) of the cases including Ag

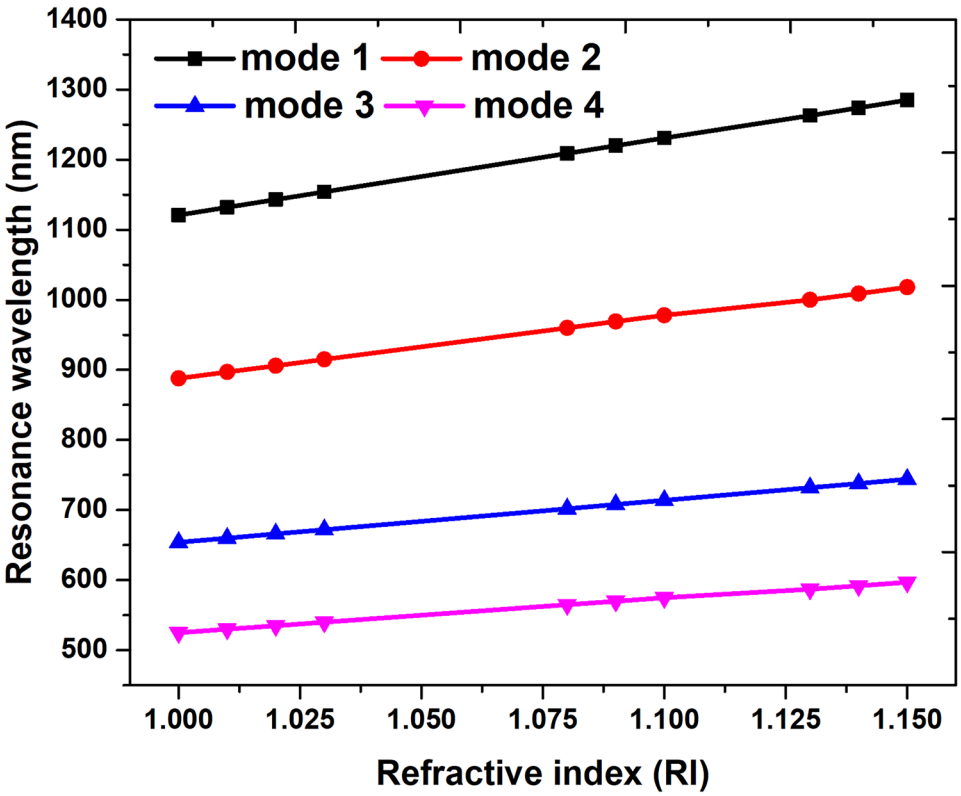

Fig. 6 Calculated resonance wavelength (λ_{res}) from mode 1 to mode 4 for the cases including Ag baffles versus refractive index (n)

baffles in the BT cavities. As seen, there is a linear relationship between λ_{res} and n. The λ_{res} increases linearly by varying the refractive index, and we can see an apparent redshift. A small variation of n can lead to an enormous shift in λ_{res}. A redshift of λ_{res} with the increase in the value of n is most significant for mode 1 compared with other modes. Consequently, the value of n can obtain from λ_{res} based on its linear relationship obtained from Eq. (2). This result demonstrates the characteristics of the sensing function of our proposed structure as a refractive index sensor. We can summarize the S and FOM of the case excluding and including Ag baffles from modes 1 to 4 in Table 1.

Compared with the case excluding Ag baffle, Ag baffles' existence in the BT cavities generates an increase of device's sensitivity by 57.14% for mode 1 and 28.57% for mode 2, correspondingly. Note that a very sharp transmittance peak (i.e., high resolution or narrow FWHM) can be seen in Fig. 4b, yielding a high Q factor. The calculated

Table 1 The S and FOM of the case excluding Ag baffle and the case including Ag baffles in BT cavities from mode 1 to mode 4

		Mode 1	Mode 2	Mode 3	Mode 4
Excluding Ag baffles	S (nm/RIU)	700.00	700.00	600.00	400.00
	FOM (RIU^{-1})	23.33	70.00	60.00	40.00
Including Ag baffles	S (nm/RIU)	1100.00	900.00	600.00	500.00
	FOM (RIU^{-1})	27.25	90.00	60.00	50.00

average Q factors are 28.02, 98.67, 109.00, and 105.00 in modes 1 to 4 of the case including Ag baffles. The proposed structure with the features of high sensitivity, FOM, and Q factors can transfer the desirable wavelength-noise-limited performance, which is attributed to the sharp transmittance peaks and results in acceptable spectral resolution.

The transmittance features of the proposed plasmonic sensor system can be affected by its structural parameters by changing the size of structural parameters, leading to a variation of ℓ_{eff} and n_{eff}. The resonance wavelength will be changed to keep the phase match condition if the resonant cavity's environment is varied [73]. Next, we will inspect the impact of structural parameters on sensitivity and figure of merit from mode 1 to mode 3, summarized in Tables S1, S2, and S3 in supplementary information and Table 2, respectively. As observed in Tables S1, S2, and S3, the influence of coupling distance between bus waveguides and BT cavities (g), bottom length of the BT cavity (L), and coupling distance among each BT cavity (d) appears to have little influence on sensitivity performance. At the same time, the FOM exhibits a different value because of the different FWHM. It is worth noting that the variation of Ag baffle's size (i.e., x-direction width of pair 1 and y-direction width of pair 2) can significantly improve the sensitivity when their size increases from 20 to 100 nm. The Ag baffles' size plays a potential role in enhancing EM waves in the narrow region of the BT cavities. Simulation results (not shown) reveal that

Table 2 The influence of each baffle's size (i.e., *x*-direction size of pair 1 and *y*-direction size of pair 2) on sensitivity and figure of merit from mode 1 to mode 3. The other structural parameters referred to Fig. 1 are $w = 50$ nm, $g = 10$ nm, and $d = 10$ nm, respectively

	Baffle's width (nm)	20	50	70	90	100
Mode 1	S (nm/RIU)	1100	1100	1200	1300	1500
	FOM (RIU^{-1})	18.18	27.25	48.00	52.00	50.00
Mode 2	S (nm/RIU)	800	900	1100	1000	1400
	FOM (RIU^{-1})	80.00	90.00	36.67	60.00	46.67.00
Mode 3	S (nm/RIU)	600	600	1000	800	1100
	FOM (RIU^{-1})	33.33	60.00	40.00	53.33	36.67

λ_{res} redshifts with the increased baffle's size, which results in a higher sensitivity to the variation of baffle's size than the other structural parameters (i.e., g, L, and d). In Table 2, the highest sensitivity can achieve $S = 1500.00$, 1400.00, and 1100.00 nm/RIU along with the high FOM = 50.00, 46.67, and 36.67 RIU^{-1} from mode 1 to mode 3, respectively. These results offer the highest mode sensitivity since the large shift of λ_{res} when exposed to a little variation in the medium refractive index. The sensitivity obtained from mode 1 to mode 3 can simultaneously reach above 1100.00 nm/RIU in the wavelength range of visible and near-infrared that is considerably greater than that of previously reported sensor designs. Note that a suitable modifying of the Ag baffle's size in the BT cavities can dramatically increase the sensitivity and FOM of the proposed structure excluding increasing the BT cavity size. Table 3 summarizes the comparisons among several published sensitivity and FOM values for diverse MIM-based sensor designs. The high quantity of sensitivity attained in the proposed structure gives a path toward optical on-chip sensors.

Application as a Glucose Sensor

Comprehending optical features of liquid (e.g., water or glucose) is considerable for solving problems in medical optics and biosensors. As a result, the SPPs could be resonant at varied wavelengths due to their changing of refractive index. For nano-medicine applications, it is crucial to develop a sensor structure to monitor the glucose concentrations. With the capability to detect the refractive index's little changes, plasmonic sensors can serve as various biomedical analyte sensing [79, 80]. The SPP modes in the proposed plasmonic MIM BT cavity sensor system are a promising candidate for efficiently inspecting the glucose value [81]. In the simulations, we can describe the refractive index of the glucose solution as [46, 82]:

$$n_g = 0.00011889 \times c_g + 1.33230545 \tag{3}$$

c_g denotes the glucose concentration (g/L) and n_g represents the glucose concentration's refractive index. Equation (3) describes the linear relationship between the c_g and n_g. A relationship can be built between n_g and λ_{res} through FEM simulations since the variation of λ_{res} also varies the n_g. Figure 7 depicts the transmittance spectrum of the solution of mode 1 to mode 4 when the glucose concentration, c_g, varies from 0 g/L, 120 g/L to 240 g/L, respectively. When the c_g increases, the n_g increases from 1.33230545 to 1.36083905 based on Eq. (3). As seen, all curves reveal the linear relations with c_g. For comparison, the structural parameters are the same as those used in Fig. 5b. As shown in Fig. 7, the λ_{res} are red-shifted with the increasing c_g. In these cases, the calculated sensitivity from mode 1 to mode 4 can reach $S = 1100$, 900, 600, and 500 nm/RIU, respectively, which are in good agreement with the results obtained from Figs. 6 and 8.

Table 3 Comparison of the sensitivity and FOM between this work and some other published works

Reference/year	Structure	Sensitivity (nm/RIU)/operating wavelength range	FOM (1/RIU)
[74]/2015	Induced transparency resonator	733/700 nm $< \lambda_{res} <$ 1000 nm	30.50
[75]/2016	Coupled double rectangular cavities	596/450 nm $< \lambda_{res} <$ 800 nm	7.50
[76]/2017	Two circular cavities	840/750 nm $< \lambda_{res} <$ 1300 nm	100
[30]/2018	Side-coupled stub-hexagon resonators	550/400 nm $< \lambda_{res} <$ 800 nm	178.00
[77]/2019	Rectangular ring resonator	1367/1300 nm $< \lambda_{res} <$ 2000 nm	22.30
[78]/2020	Semi-ring shape resonator	1084/600 nm $< \lambda_{res} <$ 900 nm	57.06
This work	Bowtie cavity configuration	1500, 1400,1100/450 nm $< \lambda_{res} <$ 1500 nm	50,46.67,36.67

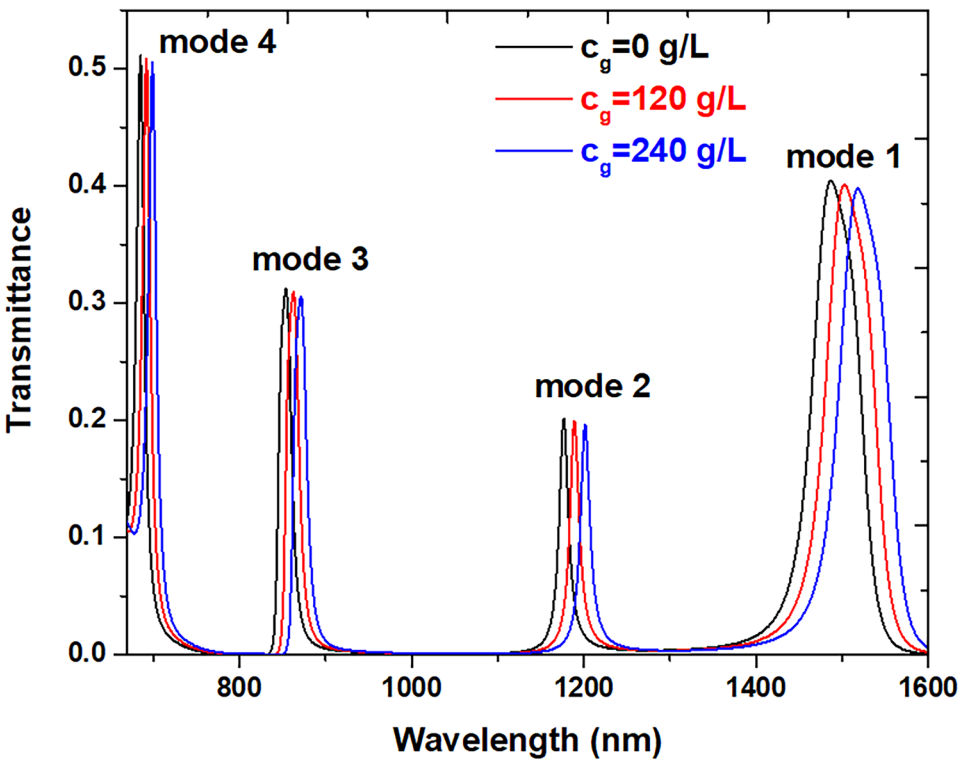

Fig. 7 Transmittance spectrum of the solution of mode 1 to mode 4 when the glucose concentration, c_g, varies from 0 g/L, 120 g/L to 240 g/L, respectively. For comparison, the structural parameters are the same as those used in Fig. 5b

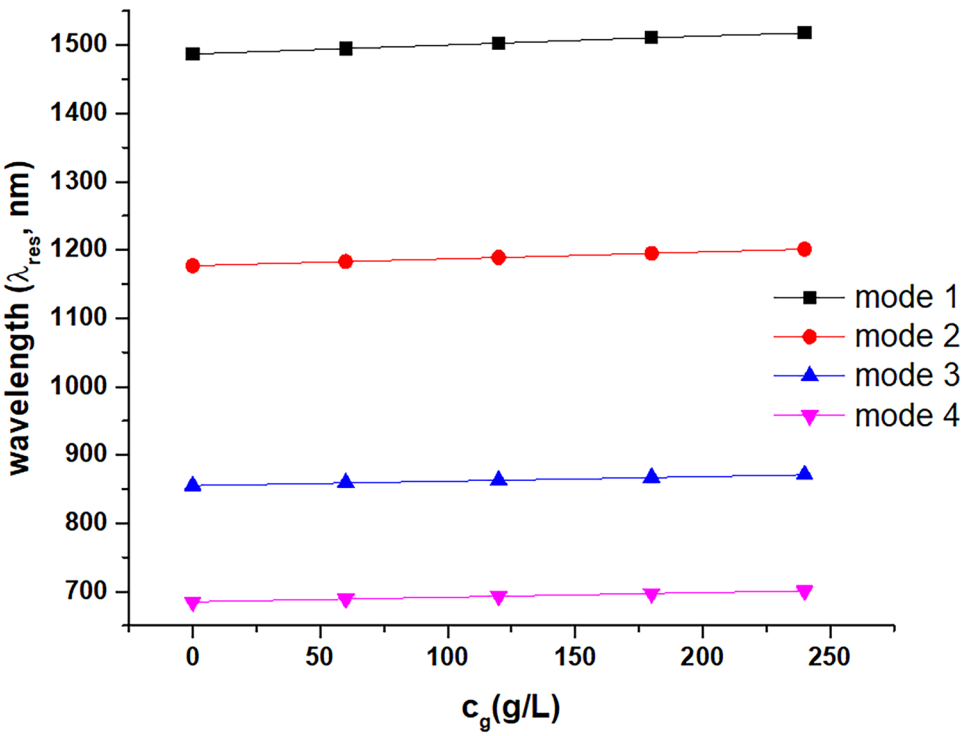

Fig. 8 Calculated resonance wavelength (λ_{res}) from mode 1 to mode 4 versus the glucose concentration (c_g) in the range from 0 to 240 g/L

Conclusion

This study proposes a new design strategy of a plasmonic sensor with multi-mode based on MIM-BT cavity configuration working in visible and infrared for refractive index and glucose sensing applications. Finite element method was used to simulate the influence of the BT cavities' geometrical parameters on the fine structure of transmittance spectra and sensor performance. Ag baffles in BT cavities can effectively adjust multiple resonant modes, which considerably raise the sensitivity by 57.14% for mode 1 compared with its counterpart excluding Ag baffles. Variation of the baffle's width (see Table 2) results in the appearance of remarkable resonance wavelength shift towards longer wavelength, which provides the highest mode sensitivity since the large change of resonance wavelength when exposed to a little variation in the medium refractive index. This research offers the theoretical foundation for comparing designs for guided nanostructures that enable the measurement of a wide variety of refractive index medium and analytes. The high sensitivity of 1500 nm/RIU and FOM of 50.00 RIU^{-1} can be achieved. We believe that the proposed structure can find significant applications in the future optical sensing domain.

Supplementary Information The online version contains supplementary material available at https://doi.org/10.1007/s11468-021-01431-8.

Author Contribution Only the single author has the contribution to this work.

Funding This research was supported by the University Research Grant of Universiti Brunei Darussalam (Grant No. UBD/RSCH/1.9/FICBF(b)/2019/006).

Data Availability All the data and material are in the manuscript.

Declarations

Ethics Approval This material is the author' own original work, which has not been previously published elsewhere.

Consent to Participate This is a theoretical study on the design of a plasmonic sensor.

Consent for Publication The author of this paper agrees to publish this work.

Conflict of Interests The author declares no competing interests.

References

1. El Kabbash M, Rahimi Rashed A, Sreekanth KV, De Luca A, Infusino M, Strangi G (2016) Plasmon-exciton resonant energy transfer: across scales hybrid systems. J Nanomater 2016:4819040
2. Ho YZ, Chen WT, Huang Y-W, Wu PC, Tseng ML, Wang YT, Chau Y-F, Tsai DP (2012) Tunable plasmonic resonance arising from broken-symmetric silver nanobeads with dielectric cores. J Opt 14:114010
3. Hsieh L-Z, Chau Y-FC, Lim CM, Lin M-H, Huang HJ, Lin C-T, NurSyafi'ie MI, M (2016) Metal nano-particles sizing by thermal annealing for the enhancement of surface plasmon effects in thin-film solar cells application. Opt Commun 370:85–90
4. Huang Y-W, Chen WT, Wu PC, Fedotov V, Savinov V, Ho YZ, Chau Y-F, Zheludev NI, Tsai DP (2012) Design of plasmonic toroidal metamaterials at optical frequencies. Opt Express 20:1760–1768
5. Chung-Ting Chou C, Yuan-Fong Chou C, Hai-Pang C (2020) Highly Sensitive Metal-Insulator-Metal Plasmonic Refractive Index Sensor with a Centrally Coupled Nanoring Containing Defects. J Phys D Appl Phys
6. Tsai D-P (2020) Exploring the electromagnetic information of metasurfaces. National Sci Rev 7:1845–1846
7. Su D-S, Tsai DP, Yen T-J, Tanaka T (2019) Ultrasensitive and selective gas sensor based on a channel plasmonic structure with an enormous hot spot region. ACS Sensors 4:2900–2907
8. Lai Y-C, Kuang TC, Cheng BH, Lan Y-C, Tsai DP (2017) Generation of convergent light beams by using surface plasmon locked Smith-Purcell radiation. Sci Rep 7:11096
9. Chou Chao C-T, Chou Chau Y-F, Chiang H-P (2020) Enhancing plasmonic effect in periodic nanometal square prisms with fences and cavities for refractive index and temperature sensing applications. J Nanoparticle Res 22:297
10. Chou Chau Y-F, Chou Chao C-T, Huang HJ, Kooh MRR, Kumara NTRN, Lim CM, Chiang H-P (2020) Ultrawide bandgap and high sensitivity of a plasmonic metal-insulator-metal waveguide filter with cavity and baffles. Nanomaterials 10:2030
11. Danaie M, Shahzadi A (2019) Design of a high-resolution metal–insulator–metal plasmonic refractive index sensor based on a ring-shaped Si resonator. Plasmonics 14:1453–1465
12. Han Z, Van V, Herman WN, Ho PT (2009) Aperture-coupled Mim plasmonic ring resonators with sub-diffraction modal volumes. Opt Express 17:12678–12684
13. Lu H, Wang G, Liu X (2013) Manipulation of Light in Mim Plasmonic Waveguide Systems. Chin Sci Bull 58:
14. Luo S, Li B, Xiong D, Zuo D, Wang X (2017) A High Performance Plasmonic Sensor Based on Metal-Insulator-Metal Waveguide Coupled with a Double-Cavity Structure. Plasmonics 12:
15. Rahmatiyar M, Afsahi M, Danaie M (2020) Design of a Refractive Index Plasmonic Sensor Based on a Ring Resonator Coupled to a Mim Waveguide Containing Tapered Defects. Plasmonics 15:
16. Matsuzaki Y, Okamoto T, Haraguchi M, Fukui M, Nakagaki M (2008) Characteristics of gap plasmon waveguide with stub structures. Opt Express 16:16314–16325
17. Lu H, Wang G, Liu X (2013) Manipulation of light in Mim plasmonic waveguide systems. Chin Sci Bull 58:3607–3616
18. Xiang D, Li W (2014) Mim plasmonic waveguide splitter with tooth-shaped structures. J Mod Opt 61:222–226
19. Kamada S, Okamoto T, El-Zohary SE, Haraguchi M (2016) Design optimization and fabrication of Mach-Zehnder interferometer based on Mim plasmonic waveguides. Opt Express 24:16224–16231
20. Xie Y, He C, Li J, Song T, Zhang Z, Mao Q (2016) Theoretical Investigation of a Plasmonic Demultiplexer in Mim Waveguide Crossing with Multiple Side-Coupled Hexagonal Resonators. IEEE Photonics J PP:1–1
21. Neutens P, Lagae L, Borghs G, Van Dorpe P (2012) Plasmon filter and resonator in metal-insulator-metal waveguides. Opt Express 20:3408–3423
22. Pu M, Yao N, Hu C, Xin X, Zhao Z, Wang C, Luo X (2010) Directional coupler and nonlinear Mach-Zehnder interferometer based on metal-insulator-metal plasmonic waveguide. Opt Express 18:21030–21037

23. Butt A, Khonina S, Kazanskiy N (2020) Highly sensitive refractive index sensor based on plasmonic bow tie configuration. Photonic Sens 10:223–232
24. Chou Chao C-T, Chou Chau Y-F, Huang HJ, Kumara N, Kooh MRR, Lim CM, Chiang H-P (2020) Highly sensitive and tunable plasmonic sensor based on a nanoring resonator with silver nanorods. Nanomaterials 10:1399
25. Chou Chau Y-F, Chou Chao C-T, Chiang H-P (2020) Ultra-broad bandgap metal-insulator-metal waveguide filter with symmetrical stubs and defects. Results Phys 17:103116
26. Chou Chau Y-F, Chou Chao C-T, Huang HJ, Kumara N, Lim CM, Chiang H-P (2019) Ultra-high refractive index sensing structure based on a metal-insulator-metal waveguide-coupled T-shape cavity with metal nanorod defects. Nanomaterials 9:1433
27. Guo Z, Wen K, Hu Q, Lai W, Lin J, Fang Y (2018) Plasmonic Multichannel Refractive Index Sensor Based on Subwavelength Tangent-Ring Metal–Insulator–Metal Waveguide. Sensors 18:
28. Malmir K, Habibiyan H, Ghafoorifard H (2016) An ultrasensitive optical label-free polymeric biosensor based on concentric triple microring resonators with a central microdisk resonator. Opt Commun 365:150–156
29. Nejat M, Nozhat N (2020) Multi-band Mim refractive index biosensor based on Ag-air grating with equivalent circuit and T-matrix methods in near-infrared region. Sci Rep 10:6357
30. Wu C, Ding H, Huang T, Wu X, Chen B, Ren K, Fu S (2018) Plasmon-induced transparency and refractive index sensing in side-coupled stub-hexagon resonators. Plasmonics 13:251–257
31. Zhang Z, Yang J, He X, Zhang J, Huang J, Chen D, Han Y (2018) Plasmonic Refractive Index Sensor with High Figure of Merit Based on Concentric-Rings Resonator. Sensors (Basel) 18:
32. Chau Y-F, Jiang Z-H (2011) Plasmonics effects of nanometal embedded in a dielectric substrate. Plasmonics 6:581–589
33. Chau Y-F, Yeh H-H, Tsai DP (2009) Surface plasmon effects excitation from three-pair arrays of silver-shell nanocylinders. Phys Plasmas 16:022303
34. Chau Y-FC, Syu J-Y, Chao C-TC, Chiang H-P, Lim CM (2016) Design of crossing metallic metasurface arrays based on high sensitivity of gap enhancement and transmittance shift for plasmonic sensing applications. J Phys D Appl Phys 50:045105
35. Chen WT, Wu PC, Chen CJ, Chung H-Y, Chau Y-F, Kuan C-H, Tsai DP (2010) Electromagnetic energy vortex associated with subwavelength plasmonic Taiji marks. Opt Express 18:19665–19671
36. Chou Chau Y-F, Lim CM, Lee C, Huang HJ, Lin C-T, Kumara N, Yoong VN, Chiang H-P (2016) Tailoring surface plasmon resonance and dipole cavity plasmon modes of scattering cross section spectra on the single solid-gold/gold-shell nanorod. J Appl Phys 120:093110
37. Chu Y, Schonbrun E, Yang T, Crozier KB (2008) Experimental observation of narrow surface plasmon resonances in gold nanoparticle arrays. Appl Phys Lett 93:181108
38. Kurokawa Y (2007) Metal-Insulator-Metal Plasmon Nanocavities: Analysis of Optical Properties. Phys Rev B 75.
39. Janković N, Cselyuszka N (2019) High-resolution plasmonic filter and refractive index sensor based on perturbed square cavity with slits and orthogonal feeding scheme. Plasmonics 14:555–560
40. Wen K, Hu Y, Chen L, Zhou J, Lei L, Guo Z (2014) Fano resonance with ultra-high figure of merits based on plasmonic metal-insulator-metal waveguide. Plasmonics 10:27–32
41. Chou Chau Y-F, Chou Chao C-T, Rao J-Y, Chiang H-P, Lim CM, Lim RC, Voo NY (2016) Tunable optical performances on a periodic array of plasmonic bowtie nanoantennas with hollow cavities. Nanoscale Res Lett 11:411
42. Xiang Z, Wang L, Wang L, Li X-F, Huang W-Q, Wen S-C, Fan D-Y (2013) Tuning bandgap of a double-tooth-shaped Mim waveguide filter by control widths of the teeth. J Opt 15:5008
43. Zhou J, Chen H, Zhang Z, Tang J, Cui J, Xue C, Yan S-B (2017) Transmission and refractive index sensing based on fano resonance in Mim waveguide-coupled trapezoid cavity. AIP Adv 7:015020
44. Zhang Z, Ma L-J, Gao F, Zhang Y-J, Tang J, Cao H-L, Zhang B-Z, Wang J-C, Yan S-B, Xue C-Y (2017) Plasmonically induced reflection in metal–insulator–metal waveguides with two silver baffles coupled square ring resonator. Chin Phys B 26:124212
45. Han Z, Bozhevolnyi SI (2012) Radiation guiding with surface plasmon polaritons. Rep Prog Phys 76:016402
46. Lo Y-L, Yu T-C (2006) A polarimetric glucose sensor using a liquid-crystal polarization modulator driven by a sinusoidal signal. Opt Commun 259:40–48
47. Hepp S, Bauer S, Hornung F, Schwartz M, Portalupi SL, Jetter M, Michler P (2018) Bragg grating cavities embedded into nanophotonic waveguides for Purcell enhanced quantum dot emission. Opt Express 26:30614–30622
48. Rakhshani M, Mansouri-Birjandi M (2017) Utilizing the Metallic Nano-Rods in Hexagonal Configuration to Enhance Sensitivity of the Plasmonic Racetrack Resonator in Sensing Application. Plasmonics 12
49. Yun B, Hu G, Zhang R, Yiping C (2016) Fano resonances in a plasmonic waveguide system composed of stub coupled with a square cavity resonator. J Opt 18:055002
50. Kaniber M, Schraml K, Regler A, Bartl J, Glashagen G, Flassig F, Wierzbowski J, Finley JJ (2016) Surface plasmon resonance spectroscopy of single bowtie nano-antennas using a differential reflectivity method. Sci Rep 6:23203
51. Roxworthy BJ, Ko KD, Kumar A, Fung KH, Chow EKC, Liu GL, Fang NX, Toussaint KC (2012) Application of plasmonic bowtie nanoantenna arrays for optical trapping, stacking, and sorting. Nano Lett 12:796–801
52. Wang B, Singh SC, Lu H, Guo C (2020) Design of aluminum bowtie nanoantenna array with geometrical control to tune Lspr from Uv to near-Ir for optical sensing. Plasmonics 15:609–621
53. Ding W, Bachelot R, Kostcheev S, Royer P, Lamaestre REd (2010) Surface plasmon resonances in silver bowtie nanoantennas with varied bow angles. J Appl Phys 108:124314
54. Ruan Z, Fan S (2010) Temporal coupled-mode theory for fano resonance in light scattering by a single obstacle. J Phys Chem C 114:7324–7329
55. Chou Chao C-T, Chou Chau Y-F, Chiang H-P (2021) Highly sensitive metal-insulator-metal plasmonic refractive index sensor with a centrally coupled nanoring containing defects. J Phys D Appl Phys 54:115301
56. El Haffar R, Farkhsi A, Mahboub O (2020) Optical properties of Mim plasmonic waveguide with an elliptical cavity resonator. Appl Phys A 126:486
57. Bahramipanah M, Abrishamian MS, Mirtaheri SA, Liu J-M (2014) Ultracompact plasmonic loop-stub notch filter and sensor. Sensors Actuat B: Chem 194:311–318
58. Chau Y-F, Lin Y-J, Tsai DP (2010) Enhanced surface plasmon resonance based on the silver nanoshells connected by the nanobars. Opt Express 18:3510–3518
59. Chau Y-F, Yeh H-H (2011) A comparative study of solid-silver and silver-shell nanodimers on surface plasmon resonances. J Nanopart Res 13:637–644
60. Chen W-C, Cardin A, Koirala M, Liu X, Tyler T, West KG, Bingham CM, Starr T, Starr AF, Jokerst NM, Padilla WJ (2016) Role of surface electromagnetic waves in metamaterial absorbers. Opt Express 24:6783–6792
61. Sun Y-S, Chau Y-F, Yeh H-H, Tsai DP (2008) Highly birefringent index-guiding photonic crystal fiber with squeezed differently sized air-holes in cladding. Jpn Appl Phys 47:3755
62. Yang K-Y, Chau Y-F, Huang Y-W, Yeh H-Y, Ping Tsai D (2011) Design of high birefringence and low confinement loss photonic

crystal fibers with five rings hexagonal and octagonal symmetry air-holes in fiber cladding. J Appl Phys 109:093103
63. Johnson PB, Christy RW (1972) Optical constants of the noble metals. Phys Rev B 6:4370–4379
64. Chen C, Oh S-H, Li M (2020) Coupled-mode theory for plasmonic resonators integrated with silicon waveguides towards mid-infrared spectroscopic sensing. Opt Express 28:2020–2036
65. Woolf D, Loncar M, Capasso F (2009) The forces from coupled surface plasmon polaritons in planar waveguides. Opt Express 17:19996–20011
66. Vieu C, Carcenac F, Pépin A, Chen Y, Mejias M, Lebib A, Ferlazzo L, Couraud L, Launois H (2000) Electron beam lithography: resolution limits and applications. Appl Surf Sci 164:111–117
67. Chen Y (2015) Nanofabrication by electron beam lithography and its applications: a review. Microelectron Eng 135:57–72
68. Zhang ZD, Wang RB, Zhang ZY, Tang J, Zhang WD, Xue CY, Yan SB (2017) Electromagnetically induced transparency and refractive index sensing for a plasmonic waveguide with a stub coupled ring resonator. Plasmonics 12:1007–1013
69. Butt MA, Kazanskiy NL, Khonina SN (2020) Highly sensitive refractive index sensor based on plasmonic bow tie configuration. Photonic Sens 10:223–232
70. Butt MA, Khonina SN, Kazanskiy NL (2020) An array of nanodots loaded Mim square ring resonator with enhanced sensitivity at Nir wavelength range. Optik 202:163655
71. Sung MJ, Ma YF, Chau YF, Huang DW (2010) Plasmon field enhancement in silver core-protruded silicon shell nanocylinder illuminated with light at 633 Nm. Appl Opt 49:6295–6301
72. Sung M-J, Ma Y-F, Chau Y-F, Huang D-W (2010) Surface plasmon resonance in a hexagonal nanostructure formed by seven core shell nanocylinders. Appl Opt 49:920–926
73. Zeng X, Hu H, Gao Y, Ji D, Zhang N, Song H, Liu K, Jiang S, Gan Q (2015) Phase change dispersion of plasmonic nano-objects. Sci Rep 5:12665
74. Ni B, Chen X, Xiong D, Liu H, Hua G, Chang J, Zhang J, Zhou H (2015) Infrared plasmonic refractive index-sensitive nanosensor based on electromagnetically induced transparency of waveguide resonator systems. Opt Quant Electron 47:1339–1346
75. Zhang Z, Luo L, Xue C, Zhang W, Yan S (2016) Fano resonance based on metal-insulator-metal waveguide-coupled double rectangular cavities for plasmonic nanosensors. Sensors 16:642
76. Liu X, Wu D, Chang Q, Zhou J, Zhang Y, Wang Z (2017) Grooved nanoplate assembly for rapid detection of surface enhanced Raman scattering. Nanoscale 9:15390–15396
77. Butt MA, Khonina SN, Kazanskiy NL (2019) Plasmonic refractive index sensor based on metal–insulator-metal waveguides with high sensitivity. J Mod Opt 66:1038–1043
78. Kazanskiy NL, Butt MA, Khonina SN (2020) Nanodots decorated Mim semi-ring resonator cavity for biochemical sensing applications. Photonics Nanostructures - Fundam Appl 42:100836
79. Li M, Cushing SK, Wu N (2015) Plasmon-enhanced optical sensors: a review. Analyst 140:386–406
80. Jiang J, Wang X, Li S, Ding F, Li N, Meng S, Li R, Qi J, Liu Q, Liu GL (2018) Plasmonic Nano-Arrays for Ultrasensitive Bio-Sensing Nanophotonics 7:1517–1531
81. Rakhshani MR, Tavousi A, Mansouri-Birjandi MA (2018) Design of a plasmonic sensor based on a square array of nanorods and two slot cavities with a high figure of merit for glucose concentration monitoring. Appl Opt 57:7798–7804
82. Yeh Y-L (2008) Real-time measurement of glucose concentration and average refractive index using a laser interferometer. Opt Lasers Eng 46:666–670